JOURNAL OF COMPUTATIONAL PHYSICS 119, 34–45 (1995)

Divergence Preserving Discrete Surface Integral Methods for Maxwell's Curl Equations Using Non-orthogonal Unstructured Grids*

NIEL K. MADSEN

Engineering Research Division, Lawrence Livermore National Laboratory, Livermore, California 94550 and Research Institute for Advanced Computer Science, NASA Ames Research Center, Moffett Field, California 94035

Received March 13, 1992

Several new discrete surface integral methods for solving Maxwell's equations in the time-domain are presented. These methods, which allow the use of general non-orthogonal mixed-polyhedral unstructured grids, are direct generalizations of the canonical staggered-grid finite difference method. These methods are conservative in that they locally preserve "divergence" or charge. Employing mixed polyhedral cells (hexahedral, tetrahedral, etc.), these methods allow more accurate modeling of non-rectangular structures and objects because the traditional "stair-stepped" boundary approximations associated with the orthogonal grid based finite difference methods can be avoided. Numerical results demonstrating the accuracy of these new methods are presented. © 1995 Academic Press, Inc.

INTRODUCTION

The solution of physical problems whose behavior is governed by Maxwell's equations has been of considerable interest for many years. The propagation of electromagnetic signals such as microwaves for communication or radar pulses for the detection of aircraft are two examples of such problems. The conventional approach for numerically solving Maxwell's equations in the time domain has been the use of finite difference methods (FDTD) in conjunction with orthogonal grids [1–5]. It is well known that the use of such methods can produce very accurate results (particularly when the domain is rectangular or almost rectangular). However, many problems involve domains or objects which are sufficiently irregular in their shapes that they cannot be easily approximated with grids consisting of orthogonal cells [6].

Over the past years a number of approaches have been developed to treat problems with irregular shapes or boundaries. The simplest of these approaches has been to use the standard FDTD algorithm and to replace the curved and irregular boundaries with "stair-stepped" approximations. This approach has worked well in some cases but can give rather poor approximations in others, unless very fine discretizatons are used [6]. Another approach has been to map the original irregular domain into a rectangular one and then to apply the FDTD method in the transformed coordinates [7, 8]. This approach suffers from the facts that more complicated equations must be solved and appropriate mapping functions are not always easily obtained. These approaches have been motivated by a desire to retain the use of the basic orthogonal grid FDTD method. The FDTD method has a number of attractive numerical properties. It is charge or divergence preserving both locally and globally. It is second-order accurate and non-dissipative. It is also very computationally inexpensive.

More recently, other numerical algorithms which allow the use of unstructured and irregular grids have been studied. Finite element methods, which have been very successfully used for solving elliptic and parabolic partial differential equations, have been used with Maxwell's equations [9, 10]. These methods allow the use of boundary conforming non-orthogonal and unstructured grids which give one the ability to approximate irregular boundaries with much greater geometrical accuracy. These methods usually provide for global charge or divergence conservation but not for local element charge conservation. When applied on orthogonal structured grids, these methods do not reduce to the familiar FDTD method. In fact, some of the finite element methods, when used with orthogonal grids, reduce to methods which have known difficulties such as grid decoupled solutions [9].

In a desire to use the FDTD algorithm essentially everywhere in a problem and still be able to match irregular boundaries, Taflove [11] has developed an approximation technique that allows the use of special non-orthogonal cells immediately adjacent to the irregular boundary. Local conservation of charge for these special boundary cells is not preserved and second-order accuracy is not assured in general. The primary advantage of this approach is that of very low computational cost. Long term stability of the method is also an open question.

* Work performed under the auspices of the U.S. Department of Energy by the Lawrence Livermore Laboratory under Contract W-7405-ENG-48. The U.S. Government's right to retain a nonexclusive royalty-free license in and to the copyright covering this paper, for governmental purposes, is acknowledged.

0021-9991/95 $6.00
Copyright © 1995 by Academic Press, Inc.
All rights of reproduction in any form reserved.

Drawing upon experience in computational fluid dynamics (CFD), finite volume methods have recently been introduced to electromagnetics [12]. These methods use flux matching techniques across cell faces to form approximations to Maxwell's equations. In order to achieve stability, these methods require the use of time integration methods which are dissipative. Lax–Wendroff or upwind time differencing methods have typically been used. These methods preserve charge or divergence only to the truncation error level. Even though accurate short time solutions have been demonstrated, there remain accuracy questions. The longer term effects of the dissipative time integration methods and the effects of the lack of exact charge conservation are questions that remain to be answered. These methods also do not reduce to the FDTD method when orthogonal grids are used.

Not related to the above-mentioned CFD-based finite volume methods, but sharing a similar name, modified finite volume (MFV) methods have been recently presented [13]. These methods again allow the use of unstructured non-orthogonal boundary confirming grids and reduce to the traditional FDTD method when used with structured orthogonal grids. These methods are charge conservative and non-dissipative and can produce very accurate solutions. Our first impression of these methods was that they had all of the desirable numerical approximation properties (charge conservation, non-dissipative, direct generalizations of FDTD, etc.). However, for some problems using highly distorted grids, weak instabilities and subsequent non-physical solution growth have been observed.

With a continuing goal of developing algorithms without significant drawbacks for solving Maxwell's equations using unstructured non-orthogonal grids, we seek algorithms which have the following properties:

1. Allow the use of unstructured non-orthogonal grids.
2. Allow a variety of cell or element types.
3. Reduce to the FDTD method when orthogonal grids are used.
4. Preserve charge or divergence locally (and globally).
5. Conditionally stable.
6. Non-dissipative.
7. Accurate for non-orthogonal grids.

In this paper we will present three new algorithms which meet the above criteria. These methods are derived using a discrete surface integration (DSI) technique. One might refer to these methods as finite volume methods, as they are derived from an integration technique. However, since they involve only surface integrations, we prefer the terminology of discrete surface integration techniques. As formulated, the DSI techniques can be used with essentially arbitrary unstructured grids composed of convex polyhedral cells. In our implementation of the DSI algorithms, we allow for the use of unstructured grids which are composed of combinations of non-orthogonal hexahedrons, tetrahedrons, triangular prisms, and pyramids. These new methods actually reduce to the conventional FDTD method when applied on a structured orthogonal hexahedral grid. The DSI techniques are formulated so that local (and, hence, global) conservation of charge or divergence of the fields is inherent in the algorithm and easily demonstrated. They use a leapfrog time integration technique which is conditionally stable and non-dissipative. This paper extends and improves our previous unstructured grid MFV algorithms [9, 13]. The new algorithms have comparable accuracy and overcome the stability or solution growth difficulties which occurred when the MFV algorithms were applied on highly distorted grids.

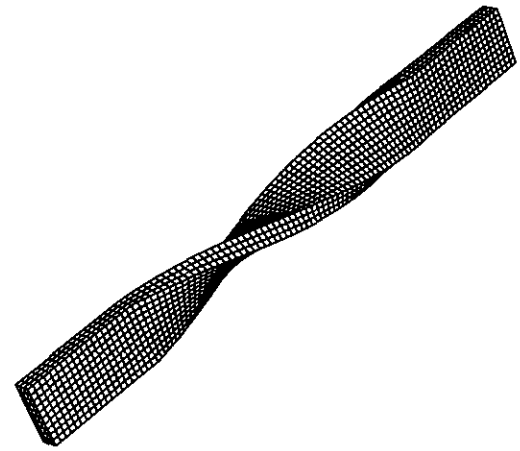

FIG. 1. Twisted waveguide discretized into hexahedral cells.

It goes without saying that algorithms based on unstructured non-orthogonal grids will be significantly more complex and costly than the orthogonal grid FDTD method. However, since the DSI methods reduce to the computationally efficient FDTD method when the grid is orthogonal, we advocate the use of grids which are orthogonal almost everywhere so that advantage may be taken of the simplifications that occur in this case. Even when non-orthogonality exists, the use of efficient data structures allow the new DSI algorithms to be quite computationally efficient.

In the next section, we will describe in detail the new DSI methods. We will then discuss issues concerning the implementation of these methods as they relate to efficiency. We will then describe the numerical experiments that have been performed to assess stability. Finally, numerical results will be presented to demonstrate the accuracy of the DSI methods.

DISCRETE SURFACE INTEGRATION METHODS

We begin by assuming that we wish to solve Maxwell's curl equations on an irregular three-dimensional domain R which has a boundary surface denoted by S. We will also assume that the domain R has been discretized into convex polyhedrons. Figure 1 shows a twisted waveguide discretized using hexahe-

dral cells. This is an example of a problem type that we wish to consider that could not be easily solved using the conventional orthogonal grid FDTD method. Maxwell's curl equations are given by

$$\frac{\partial \mathbf{D}}{\partial t} = \nabla \times \mathbf{H} \tag{1}$$

$$\frac{\partial \mathbf{B}}{\partial t} = -\nabla \times \mathbf{E}, \tag{2}$$

where for linear isotropic materials the vectors **D**, **E**, **B**, and **H** are related by the constitutive relationships

$$\mathbf{D} = \varepsilon \mathbf{E}$$

$$\mathbf{B} = \mu \mathbf{H}.$$

The linear isotropic material properties are: ε, the permittivity, and μ, the permeability. Like the conventional FDTD method, the DSI methods can be generalized to treat more complex materials. However, for the purposes of this paper, we will assume that the linear isotropic material properties are piecewise constant over the domain R. We will also assume that S is a perfectly conducting surface, i.e., $E_{\tan} = 0$. This is sufficient to guarantee that the problem is well posed.

We will derive our new DSI algorithms for unstructured grids formed from convex polyhedral cells. We restrict the choice of cell types to convex polyhedrons whose edges are straight lines. The faces of the polyhedrons are not necessarily planar and we make the assumption that any face in the assembled grid is shared by at most two cells. These are very weak restrictions and allow a great deal of flexibility.

The DSI method requires the use of a dual grid. The dual grid and its structure are completely derivable from a knowledge of the primary grid. For each cell of the primary grid, we define its barycenter to be a node of the dual grid. The barycenter of a cell is located at the average of the coordinates of the nodes which define the cell. We construct edges of the dual grid by connecting barycenters of adjacent cells with straight lines passing through each of the interior cell faces of the primary grid. The barycenters of two cells will be connected (i.e., form a dual edge) if and only if the two cells share a common face. For primary cell faces which lie on the problem boundary, S, we form a corresponding dual edge by joining the cell barycenter to the face barycenter. There is a one-to-one correspondence between the nodes, edges, faces, and cells of the primary grid to the cells, faces, edges, and nodes of the dual grid, respectively. The dual face associated with a primary edge has as its perimeter the dual edges associated with all of the primary faces which share the given primary edge. The dual cell associated with a primary node has as its surface the dual faces which correspond to all of the primary edges which share the primary node. Although not necessary for the definition of the new algorithms, we recommend that the variations in grid sizes and angles be sufficiently smooth so that the primary and dual edges actually intersect their corresponding dual and primary faces, respectively. Degradation of solution accuracy has been observed when this condition is not met. Figure 2 shows an eight cell hexahedral primary grid and its one interior dual cell.

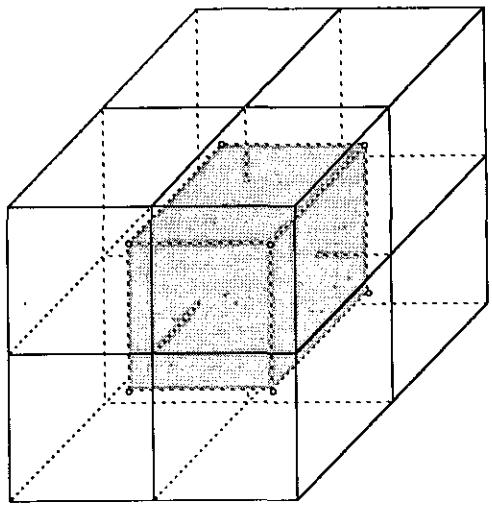

FIG. 2. Primary grid consisting of eight hexahedral cells and its one interior dual cell.

Our DSI solution variables will be associated with the edges and faces of the primary grid and also with the edges and faces of the dual grid. The quantity associated with a primary cell edge is the projection of the electric field vector onto that edge, i.e., $\mathbf{E} \cdot \mathbf{s}$, where $\mathbf{s}$ is the primary cell edge vector. The magnetic field projection $\mathbf{H} \cdot \mathbf{s}^*$ is associated with a dual cell edge, where $\mathbf{s}^*$ is the dual cell edge vector. In addition, with each primary grid face we will associate a full magnetic field vector **B**, and with each dual grid face we will associate a full electric displacement vector **D**. We will denote with an asterisk, *, the geometric quantities associated with the dual grid. Figure 3 depicts these associations. We remark that these associations of field quantities with the primary and dual grid locations are entirely reciprocal and that the respective locations of the

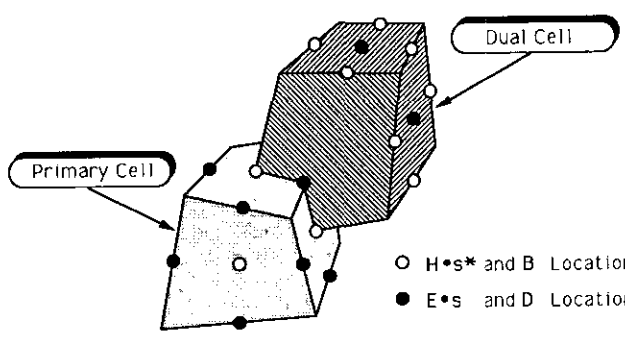

FIG. 3. Discrete electric and magnetic field variable locations relative to the primary and dual grid cells.

magnetic and electric field quantities could be interchanged. The particular choice of which field quantities to associate with each grid is best determined by deciding which field quantities one desires to have on the exterior boundary surfaces where the boundary conditions will be imposed. Since we are assuming that our domain R is surrounded by a perfect electric conductor, we will associate the electric and magnetic field quantities as described above. For open region problems, the choice for the location of the field quantities will depend on the particular radiation boundary condition algorithm used.

We will now describe the equations and algorithmic process used to advance in time the magnetic field vectors which are associated with each primary grid face. We assume that the time variable has been discretized by the choice of a timestep size, Δt. Superscripts on field quantities will denote their time state with $\mathbf{D}^k = \mathbf{D}(t^k) = \mathbf{D}(k\,\Delta t)$. As we will be using a leapfrog style time integration method, the magnetic field vectors will be associated with half-integer times, $t^{k+1/2}$, and the electric field vectors will be associated with integer times, t^k. For a particular primary cell face, we define the area-normal vector to be $\mathbf{N} = \int \mathbf{n}\, dS$, where $\mathbf{n}$ is a unit surface normal defined by the right-hand rule in relation to a specified circulation around the perimeter of the cell face. It is easily shown that $\mathbf{N}$ is uniquely determined by the perimeter of the surface and is independent of the actual interior surface shape. This fact allows for simple computations of $\mathbf{N}$ using piecewise planar approximating surfaces. Using (2) for the primary grid face, F, we define the time derivative of the normal component of the magnetic field to be

$$\frac{d\mathbf{B}^k}{dt}\cdot\mathbf{N}_F \equiv \int_F \left(\frac{\partial \mathbf{B}^k}{\partial t}\cdot\mathbf{n}\right) dS = -\int_F (\nabla\times\mathbf{E}^k)\cdot\mathbf{n}\, dS = -\oint_F \mathbf{E}^k\cdot d\mathbf{l}. \tag{3}$$

Equation (3) allows us to obtain the time derivative of the normal component of the magnetic field on a primary face, F, from the electric field projections onto the perimeter edges of that face. The last integral in (3) is easily computed numerically by summing these edge projections. This can be done for each primary cell face.

The next step in the algorithm is to use these time derivatives of the normal components of the magnetic field to compute a full vector value of $d\mathbf{B}_F^k/dt$ for the primary cell face, F. We will assume that the face F is defined by P primary edges and nodes, with the ith node being located at the intersection of the consecutive edges i and $m = (i \bmod P) + 1$. Also, we assume that the face F is shared by N_c primary grid cells, where by construction: $N_c = 1$ for boundary faces and $N_c = 2$ for interior faces. We will denote by $F_{i,j}$, the face of cell j (other than F) which shares edge i. Figure 4 depicts these associations for a dual edge associated with a primary face defined by five primary edges. At each of the P nodes of face F, we will unfold N_c vector values $d\mathbf{B}_{ij}^k/dt$ by solving the 3×3 system of equations:

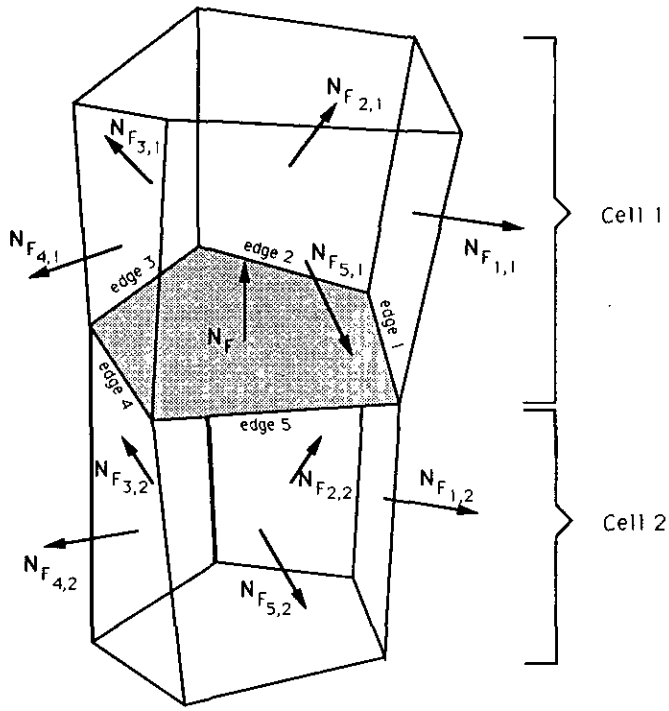

FIG. 4. Primary grid faces used to time advance a magnetic field vector.

$$\begin{aligned}
\frac{d\mathbf{B}_{ij}^k}{dt}\cdot\mathbf{N}_F &= -\oint_F \mathbf{E}^k\cdot d\mathbf{l}\\
\frac{d\mathbf{B}_{ij}^k}{dt}\cdot\mathbf{N}_{F_{i,j}} &= -\oint_{F_{i,j}} \mathbf{E}^k\cdot d\mathbf{l}\\
\frac{d\mathbf{B}_{ij}^k}{dt}\cdot\mathbf{N}_{F_{m,j}} &= -\oint_{F_{m,j}} \mathbf{E}^k\cdot d\mathbf{l},
\end{aligned} \tag{4}$$

where $i = 1, \ldots, P$, $j = 1, \ldots, N_c$, and $m = (i \bmod P) + 1$. For this primary face, F, which is shared by N_c primary cells, there are PN_c different values of $d\mathbf{B}_{ij}^k/dt$, which will now be averaged or interpolated to form a single $d\mathbf{B}_F^k/dt$ vector for the face. There are many reasonable ways to average these vectors and we will consider the three following averaging or interpolating methods:

$$\frac{d\mathbf{B}_F^k}{dt} = \left(\frac{1}{N_c P}\right)\sum_{j=1}^{N_c}\sum_{i=1}^{P}\frac{d\mathbf{B}_{ij}^k}{dt}, \tag{5a}$$

$$\frac{d\mathbf{B}_F^k}{dt} = \left(\frac{1}{N_c}\right)\sum_{j=1}^{N_c}\frac{\sum_{i=1}^{P}|w_{ij}|(d\mathbf{B}_{ij}^k/dt)}{\sum_{i=1}^{P}|w_{ij}|}, \tag{5b}$$

$$\frac{d\mathbf{B}_F^k}{dt} = \frac{\sum_{j=1}^{N_c}\sum_{i=1}^{N_c}|w_{ij}|(d\mathbf{B}_{ij}^k/dt)}{\sum_{j=1}^{N_c}\sum_{i=1}^{P}|w_{ij}|}, \tag{5c}$$

where the weight

$$w_{ij} = \mathbf{N}_F \cdot (\mathbf{N}_{F_{i,j}} \times \mathbf{N}_{F_{i+1,j}})$$

represents the volume of the j^{th} local coordinate system at node i of face F. We note also that the weight w_{ij} is the determinant of the system of Eqs. (4). A different discretization method will be obtained for each different averaging method. We characterize (5a) as a simple vector sum average, (5b) as a partially volume weighted average, and (5c) as a fully volume weighted average. As will be subsequently discussed, numerical evidence indicates a preference for the fully volume weighted averaging scheme (5c).

The full **B** vector for each primary face, F, may now be advanced in time using the time-centered leapfrog algorithm:

$$\mathbf{B}^{k+1/2} = \mathbf{B}^{k-1/2} + \Delta t \frac{d\mathbf{B}^k}{dt}, \tag{6}$$

where Δt is the specified timestep size. Finally, a time advanced value of the projection of the magnetic field onto the dual edge, $\mathbf{s}^*$, which penetrates the primary cell face, F, is easily obtained using

$$(\mathbf{H} \cdot \mathbf{s}^*)^{k+1/2} = \frac{\mathbf{B}^{k+1/2} \cdot \mathbf{s}^*}{\mu}, \tag{7}$$

where μ is an appropriate permeability value. If the permeability is discontinuous then a value can be determined by an appropriate average as is done for FDTD algorithms.

It is important to note that the first equation in (4) (namely, the equation coming from the given face F) is common to all of the sets of 3×3 equations being used in the time advance process for the face. This implies that the averaged value (5) of the time derivative of the magnetic field vector for F also satisfies this equation. It is from this aspect of the numerical algorithm that divergence or charge conservation can be demonstrated. If we integrate the divergence of (6) over a primary cell, C, we obtain

$$\begin{aligned} \int_C (\nabla \cdot \mathbf{B}^{k+1/2})\, dV &= \int_C (\nabla \cdot \mathbf{B}^{k-1/2})\, dV \\ &\quad + \Delta t \int_C \left(\nabla \cdot \frac{d\mathbf{B}^k}{dt} \right) dV. \end{aligned} \tag{8}$$

Considering the last integral term in (8) we have

$$\begin{aligned} \int_C \left(\nabla \cdot \frac{d\mathbf{B}^k}{dt} \right) dV &= \int_{\partial C} \left(\frac{d\mathbf{B}^k}{dt} \cdot \mathbf{n} \right) dS \\ &= -\sum_i \oint_{F_i} \mathbf{E}^k \cdot d\mathbf{l} = 0, \end{aligned} \tag{9}$$

where the sum runs over all the faces F_i of the closed cell C. The last sum is zero because each edge of C will be traversed twice, once in each direction. Thus we see that the local divergence of the time derivative of the magnetic field vector is zero and so if the initial fields have zero local divergence, then (8) and (9) prove that zero divergence of the time advanced fields will be conserved.

To time advance the electric field vectors which are associated with each dual cell face, we proceed in a manner which is exactly "dual" to the magnetic field procedure described above. For any dual cell face, we define the dual area-normal vector to be $\mathbf{N}^* = \int \mathbf{n}^*\, dS^*$, where $\mathbf{n}^*$ is a unit dual surface normal defined by the right-hand rule in relation to a specified circulation around the perimeter of the dual cell face. Using (1) for a given dual grid face F^*, we define the time derivative of the normal component of the electric displacement vector to be

$$\begin{aligned} \frac{d\mathbf{D}^{k+1/2}}{dt} \cdot \mathbf{N}^*_{F^*} &\equiv \int_{F^*} \left(\frac{\partial \mathbf{D}^{k+1/2}}{\partial t} \cdot \mathbf{n}^* \right) dS^* \\ &= \int_{F^*} (\nabla \times \mathbf{H}^{k+1/2}) \cdot \mathbf{n}^*\, dS^* \\ &= \oint_{F^*} \mathbf{H}^{k+1/2} \cdot d\mathbf{l}^*. \end{aligned} \tag{10}$$

Again, the last integral in (10) is easily computed by summing the projections of the magnetic field on the edges defining the dual cell face. This can be done for each dual cell face.

The next step in the algorithm is to use these time derivatives of the normal components of the electric field to compute a full vector value of $d\mathbf{D}^k_{F^*}/dt$ for the dual cell face, F^*. We will assume that the face F^* is defined by P^* dual edges and nodes, with the i^{th} dual node being located at the intersection of dual edges i and $m = (i \bmod P^*) + 1$. Also, we assume that the dual face F^* is shared by N^*_c dual cells. We will denote by $F^*_{i,j}$, the dual face of dual cell j (other than F^*) which shares dual edge i. Figure 4 with all quantities replaced by their appropriate duals would depict these associations. At each of the P^* dual nodes of dual face F^*, we will unfold N^*_c vector values $d\mathbf{D}^{k+1/2}_{ij}/dt$ by solving the 3×3 system of equations

$$\begin{aligned} \frac{d\mathbf{D}^{k+1/2}_{ij}}{dt} \cdot \mathbf{N}^*_{F^*} &= \oint_{F^*} \mathbf{H}^{k+1/2} \cdot d\mathbf{l}^* \\ \frac{d\mathbf{D}^{k+1/2}_{ij}}{dt} \cdot \mathbf{N}^*_{F^*_{i,j}} &= \oint_{F^*_{i,j}} \mathbf{H}^{k+1/2} \cdot d\mathbf{l}^* \\ \frac{d\mathbf{D}^{k+1/2}_{ij}}{dt} \cdot \mathbf{N}^*_{F^*_{m,j}} &= \oint_{F^*_{m,j}} \mathbf{H}^{k+1/2} \cdot d\mathbf{l}^*, \end{aligned} \tag{11}$$

where $i = 1, \ldots, P^*$, $j = 1, \ldots, N^*_c$, and $m = (i \bmod P^*) + 1$. For this dual face, F^*, which is shared by N^*_c dual cells, there are $P^*N^*_c$ different values of $d\mathbf{D}^{k+1/2}_{ij}/dt$, which will now be

averaged or interpolated to form a single $d\mathbf{D}_{F^*}^{k+1/2}/dt$ vector for the dual face. The averaging methods (5a)–(5c) used for the magnetic fields are also used for the electric fields.

The full $\mathbf{D}$ vector for the dual face, F^*, may now be advanced in time using the time-centered leapfrog algorithm,

$$\mathbf{D}^{k+1} = \mathbf{D}^k + \Delta t \frac{d\mathbf{D}^{k+1/2}}{dt}, \tag{12}$$

where Δt is the specified timestep size. Finally, a time advanced value of the projection of the electric field onto the primary edge, $\mathbf{s}$, which penetrates the dual cell face, F^*, is easily obtained using

$$(\mathbf{E}\cdot\mathbf{s})^{k+1/2} = \frac{\mathbf{D}^{k+1/2}\cdot\mathbf{s}}{\varepsilon}, \tag{13}$$

where ε is an appropriate permittivity value. The local conservation of divergence for the electric field can be easily shown in a manner similar to that described above for the magnetic fields.

Equations (3)–(7) for the magnetic field quantities, Eqs. (10)–(13) for the electric field quantities, and a linear averaging method (5), constitute the new divergence conserving DSI approximation methods.

When used with structured grids composed solely of hexahedral cells, the new DSI method differs only slightly from our previous MFV method. In computing the time advanced value of an edge-projected magnetic field value, exactly the same electric field values would be used to compute the required time derivative. However, slightly different weights or coefficients would be used in the DSI method. For unstructured grids, the differences between the DSI method and the MFV method become more pronounced. In general, the DSI method requires fewer dual edge magnetic field projections to time advance a given electric field projection than does the MFV method. For the DSI method, only those dual edges defining the dual faces which are immediately adjacent to the dual face of the primary grid edge being updated are used in the update algorithm. In contrast, the MFV algorithm would use the dual edges of all of the dual faces (potentially many more) of the two dual cells which surround the primary grid edge field value that is being time advanced. Thus we see that the DSI algorithm is in general more compact than is the MFV algorithm.

We note that significant simplifications occur when a primary edge is orthogonal to its dual face, or "dually," when a dual edge is orthogonal to its primary face. When this occurs, the vectors $\mathbf{s}$ and $\mathbf{N}_{F^*}^*$ (or $\mathbf{s}^*$ and $\mathbf{N}_F$) are aligned. The time advance of the edge-projected field value may be performed directly using (3) (or (10)) and the averaging (5) may be completely bypassed. Stated another way, when the above orthogonality conditions exist, the time advance of $\mathbf{E}\cdot\mathbf{s}$ (or $\mathbf{H}\cdot\mathbf{s}^*$) may be accomplished using a single line integral around the perimeter of the face F^* (or F). It is this fact that demonstrates that the DSI methods are completely equivalent to the canonical FDTD methods when orthogonal hexahedral-based grids are used. Therefore, the DSI methods are direct generalizations of the orthogonal grid FDTD methods for unstructured non-orthogonal grids. These orthogonality conditions may occur locally for only a relatively few edges or they may occur globally for the entire grid. They occur globally when structured grids composed of orthogonal hexahedral cells are used. They also occur globally when grids are used which are three-dimensional analogs of two-dimensional grids formed from Delaunay triangles and their dual Voronoi polygons. We will indicate in the next section how a properly structured code can take advantage of these simplifications when orthogonality occurs.

Exterior (perfect electric conductor) boundary conditions are very easily handled by simply setting $\mathbf{E}\cdot\mathbf{s} = E_{\tan} = 0$ for those edges $\mathbf{s}$ of the grid which form the boundary. Therefore, the above time advance procedure is not required for the electric field projections for edges which are boundary edges as these projections are determined completely from the boundary conditions. For primary cell edges which have one endpoint on the problem boundary surface S and the other in the interior of R, there will be only one complete dual cell associated with this edge (rather than two). The second dual cell is incomplete as it is clipped by the boundary surface S. For computing $\mathbf{E}\cdot\mathbf{s}$ for such edges, appropriate values for the line integrals around the incomplete dual faces can be determined from the boundary conditions using reflection principles. By choosing primary grids which are locally orthogonal near the exterior boundary, the time advance of the edge projection can be performed as mentioned above without using any of the incomplete boundary dual faces.

Local grid orthogonality at exterior boundaries also facilitates the solution of open region problems (those which are not enclosed by perfect conductors). We have not as yet developed three-dimensional radiation boundary conditions which are useable with general non-orthogonal grids. However, open region problems can be solved using the new DSI methods if the exterior boundary cells are made to be orthogonal. In this case, the radiation boundary condition methods [14] developed for the canonical FDTD methods are easily applied. Again, this is possible because of the equivalency of the DSI methods and the canonical FDTD method for orthogonal grids.

As implied in the DSI algorithm description above, interior material interfaces are also easily handled by using appropriately averaged values for the discontinuous permittivity, ε, and the permeability, μ (as is customary with the conventional orthogonal grid FDTD method).

IMPLEMENTATION OF THE DSI METHOD

In actually implementing the new DSI algorithm, there is considerable flexibility in choosing the variables to be used as the actual computational variables. If computer storage were not a significant consideration, one could keep the edge projected

values, the face normal components, and the full solution vectors associated with the faces. However, storage is almost always an issue for large three-dimensional problems and in our implementation we have chosen to use the projections of the vector fields onto the primary and dual grid edges. Direct equations for the time advance of $\mathbf{H} \cdot \mathbf{s}^*$ and $\mathbf{E} \cdot \mathbf{s}$ are easily derived by combining and manipulating (3)–(7) and (10)–(13), respectively. For an implementation using edge projected field values as the variables, the total number of unknown approximate field quantities is clearly equal to the number of cell edges in the primary grid plus the number of cell edges in the dual grid. For a non-orthogonal, but structured, hexahedral grid the time advance of a typical interior $\mathbf{E} \cdot \mathbf{s}$ will involve the use of 20 surrounding magnetic field projected values, $\mathbf{H} \cdot \mathbf{s}^*$. A similar number of electric field values would be used for the time advance of a typical magnetic field value. For orthogonal hexahedral grids, this number reduces to four. These significant potential savings are the basis for our advocating the use of orthogonal grids wherever possible. These potential savings have also motivated us to design an implementation of the algorithm which can benefit from orthogonality when it occurs.

In implementing this new DSI algorithm, we have structured the code so that there first occurs a preprocessing phase. In this phase, the dual grid is constructed from the primary grid information and a dependency graph is constructed for each primary grid and dual grid variable. A dependency graph is simply a list of pointers which point to all of the other grid variables that are required to time advance a specific grid variable. In conjunction with the dependency graph, coefficients are also generated so that any given variable may be advanced in time by computing a single very simple dot product of a coefficient vector with a vector of appropriate variables determined from the dependency graph. In forming the dependency graph, checks for orthogonality are performed and variables that are not needed for the time advance due to reasons of orthogonality are never used or stored in the dependency graph. This allows us to take advantage of the greater efficiencies (both in storage and computational arithmetic) inherent in the algorithm when grid orthogonality exists, either locally or globally. Following the preprocessing phase is the execution phase where the dependency graph, coefficients, and simple dot products are repeatedly used to time advance all of the problem variables.

We have recently been solving some rather large problems using the DSI method on unstructured grids. One particular problem involved an unstructured grid consisting of 262,620 cells, resulting in 1,645,195 degrees of freedom, and required only about 17,493,000 words of memory to execute on a Cray-2. No memory saving techniques such as word packing were used. The computational time required for this problem was about 7 μs per timestep per degree of freedom. The amount of memory and computational time required for a problem can vary significantly, depending upon the structure and orthogonality present in the problem grid.

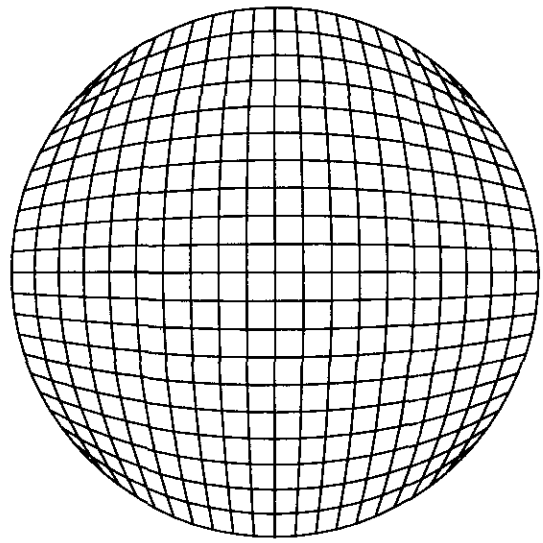

FIG. 5. Highly distorted grid obtained by mapping a 20×20 square grid to a circle.

STABILITY EXPERIMENTS

We have presented a description of three new DSI algorithms for solving Maxwell's equations. Each algorithm is distinguished by a different averaging method used to form the time derivative of a vector field associated with a cell face. As these methods reduce to be the canonical FDTD method on orthogonal grids, their stability properties (when used with this type of grid) are the same as for the FDTD methods. As we have been unable to mathematically analyze their stability properties for non-orthogonal unstructured grids, we have performed computational experiments to study this issue. While we recognize that these experiments do not conclusively demonstrate stability, we feel that they are useful to give general indications of stability characteristics.

For testing stability on highly distorted grids, we have found that a grid obtained from mapping a $10 \times 10 \times 10$ cubical grid to a sphere provides a good test. The corner cells of the cubical grid become very highly distorted under the mapping. For two-dimensional testing, a square grid mapped to a circle provides a good test. Figure 5 shows a 20×20 two-dimensional square grid mapped to a circle and it indicates the degree of distortion that occurs in the corner cells. These problems can be randomly excited and the solution can be monitored for many thousands of time steps to see if growth occurs in the solution. We judge the stability of an algorithm by measuring the solution growth over time in terms of total energy or maximum solution magnitude.

We have experimented with the three different DSI averaging methods: (5a), a simple vector sum average of all of the time derivative vectors on both sides of the given face; (5b), a vector sum average of the two volume-weighted averages of time deriv-

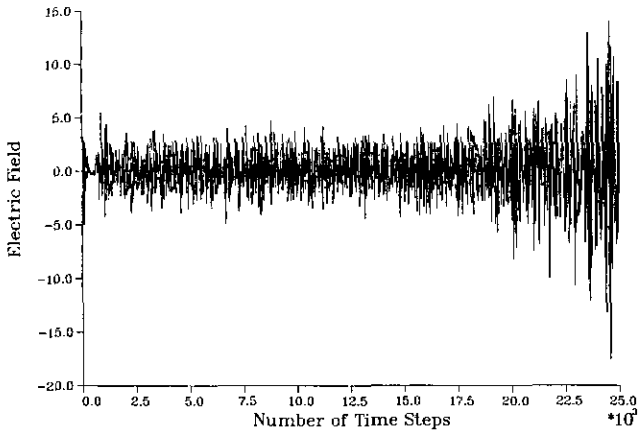

FIG. 6. Long-term solution growth plot for the weakly unstable MFV algorithm.

ative vectors on either side of the given face; and (5c), a full volume-weighted average of all of the time derivative vectors on both sides of the given face. Numerical experiments involving the use of 50,000 timesteps have indicated that all of the three DSI methods are conditionally stable. However, they differ in that they seem to have different stability limits. For the highly distorted spherical grid mentioned above, we have observed differences in the maximum allowable timestep sizes by factors as large as 5. The simple vector sum average method, (5a), always required the smallest timestep size and the full volume-weighted averaging method, (5c), allowed the largest timestep size. The mixed vector sum and volume weighted average method, (5b), always fell between the other two methods. For these stability reasons we advocate the use of the full volume weighting averaging method (5c). In contrast, our previous MFV method [13] is simply unstable for these highly distorted grids. In performing stability experiments with various algorithms, we have observed that it is essential to use a large simulation time (involving many timesteps) so as to allow enough time for signals to transit the computational domain many times. For some distorted grids, our previous MFV method would exhibit no discernible solution growth until many thousands of timesteps had occurred. Figure 6 shows an example of an MFV solved waveguide problem that showed no apparent solution growth until some 20,000 timesteps had been taken. In Fig. 6, the electric field at every tenth timestep for a single point is plotted versus the timestep number. For this same problem, the DSI algorithm does not show any spurious solution growth even to 50,000 timesteps. To determine an appropriate timestep size in solving a particular unstructured grid problem, we compute the smallest primary or dual grid edge length and divide by the local propagation velocity. We then use a timestep size which is half of this computed value. In general, this has been a reliable approach.

ACCURACY EXPERIMENTS

We feel it is important to demonstrate the accuracy of new algorithms by comparing their numerical solutions for problems which have known and computable analytic solutions. We have extensively compared the new DSI method with our previous MFV method [13]. For problems using hexahedral grids, where the MFV method does not encounter stability related solution growth, we have found that the two methods produce solutions which are almost indistinguishable. Therefore, in the results which follow, we will present results only for the full volume weighted averaging DSI method.

We first consider a simple problem which is designed to provide some assessment of the wave propagation characteristics of the new algorithm. We consider the propagation of a TE_{10} signal in a rectangular waveguide which is 1 m in width, 0.3 m in height, and 10.0 m in length. The signal is initiated in the waveguide by specifying the tangential field, E_z, at the left boundary ($y = 0.0$). The function used to drive this signal is

$$E_z(t, x, 0, z) = \sin(1.5\,\pi t)\sin(\pi x). \tag{14}$$

We assume that all of the waveguide walls are perfect electric conductors; i.e., $E_{\tan} = 0$. Normalized values for the material parameters ε and μ are used: $\varepsilon = 1.0$ and $\mu = 1.0$. The signal is allowed to propagate until $t = 8$. The analytic solution for this problem has been derived and computed so we may examine the errors precisely.

We have used a variety of grids to numerically solve this problem. Clearly one simple grid for this problem is an orthogonal hexahedral grid. However, to demonstrate the ability to use non-orthogonal grids, we deliberately skew the $10 \times 100 \times 3$ grid so that it is composed of non-orthogonal hexahedrons as shown in Fig. 7. The skewing for this grid is such that halfway down the length of the guide the cells have angles of about 57° and 123°. Figure 8 compares the time histories of the numerical solutions for the skewed and orthogonal hexahedral grids, respectively, with the analytic solution for a point in the center of the waveguide and 4.0 m down the guide. We note that the significant error occurs as the signal first reaches the observation point. Both solutions exhibit typical dispersion errors; however, the skewed grid results are somewhat better. To more precisely compare the solutions, Fig. 9 shows the maximum errors over the entire waveguide for both the skewed and

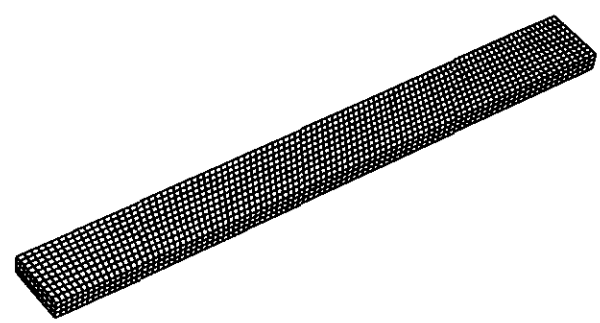

FIG. 7. Skewed $10 \times 3 \times 100$ non-orthogonal hexahedral waveguide grid.

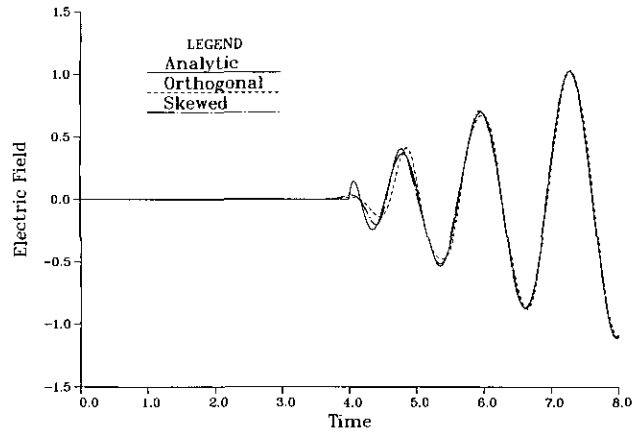

FIG. 8. Numerical TE_{10} waveguide solutions compared with the analytic solution for a point 4.0 m down the guide: (a) analytic solution; (b) orthogonal grid DSI solution; (c) skewed grid DSI solution.

orthogonal hexahedral grid solutions as a function of time. These maximum errors should be referenced to the solution magnitude which oscillates roughly between $+1$ and -1. Surprisingly, for all but the earliest times, the skewed grid produces a uniformly better solution. To demonstrate that other grid cell types can produce acceptable solutions Table I compares the maximum errors, run times in seconds for an IBM RISC 6000 Model 550 computer, and problem sizes for several different grids. The grids differ in the number of cells and edges. The non-hexahedral grids were all formed from the orthogonal and skewed hexahedral grids by subdividing each hexahedral cell into five tetrahedrons, six pyramids, two tetrahedrons, and two pyramids, or two triangular prisms. The subdivision of a single hexahedral cell into five tetrahedrons and the subdivision into two tetrahedrons and two pyramids is shown in Figs. 10–11.

From Table I one can see that the most accurate results were

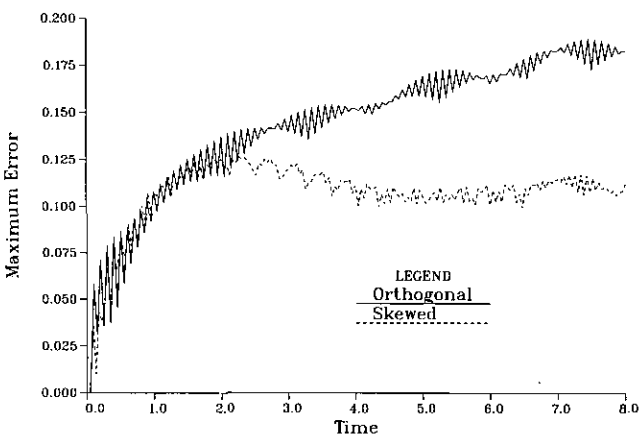

FIG. 9. Comparison of maximum errors as a function of time for the DSI orthogonal and skewed waveguide hexahedral grids.

obtained using the tetrahedral grid derived from the skewed hexahedral grid. However, these results required a great deal more computer time to obtain. The worst results resulted from the use of the skewed grid consisting of tetrahedral and pyramidal cells. The poorer results reflect the fact the grid is composed of highly distorted cells which have very large and very small internal angles. It seems apparent that this problem is most efficently solved using grids consisting of hexahedral cells.

To demonstrate the accuracy that can be gained by the better zoning of non-orthogonal surfaces than can be achieved using only orthogonal cells, we consider the problem of the scattering of a plane wave guassian pulse from a perfectly conducting sphere of radius 0.1 m. The plane-wave pulse is defined by the Gaussian-like function

$$f(t) = \begin{cases} \dfrac{\exp(-10[10^9 t - 1]^2) - \exp(-10)}{1 - \exp(-10)}, & \text{if } 0 \le t \le 2 \times 10^{-9}, \\ 0, & \text{otherwise.} \end{cases}$$

This problem again has a computable analytic solution so we may compare errors precisely. Figure 12 shows the DSI surface grid and a stair-stepped orthogonal grid approximation for the surface of a sphere of radius 0.1 m. Both surface grids are derived from a $6 \times 6 \times 6$ cubical grid. The DSI surface grid is obtained by mapping the surface of the discretized cube to a 0.1-m radius sphere. The stair-stepped orthogonal grid is obtained by eliminating cells from the cubical grid. Figure 13 compares the orthogonal grid finite difference scattered field solution and the DSI scattered field solution with the analytic solution for a point which lies in the shadow region (behind the sphere relative to the direction of the incident pulse) two sphere radii away from the sphere surface. The maximum errors are noticeably different. Significantly more accurate results are obtained by avoiding the orthogonal "stair-stepped" grids. It is also noteworthy that the DSI results were obtained using a 2.2-m diameter hemispherical domain which was discretized using only 9600 radially expanding cells. In contrast, the finite difference solution used half of a 2.0-m cubical domain with a $60 \times 60 \times 30$ uniform cubical discretization (108,000 cells).

Another problem that has a known analytic solution is that of a pulsed dipole radiating in free space. We assume that a dipole is located at the origin and is oriented in the z-direction. We will drive it for a finite amount of time with the pulsed amplitude function $f(t) = g(\alpha(t))$, where $\alpha(t) = 4 \times 10^7 - 1$ and where

$$g(x) = \begin{cases} (x^2 - 1)^4, & \text{if } -1 \le x \le 1, \\ 0, & \text{otherwise.} \end{cases}$$

As the solution of this problem depends strongly on this function

TABLE I

Comparison of TE_{10} Waveguide Solution Maximum Errors, Run Times, and Problem Sizes for Various DSI Grids

Grid type		Max error	Steps	Time	Nodes	Edges	Faces	Cells
Hexahedral	Orth	.182	160	6.7	4444	11773	10330	3000
	Skew	.112	184	8.2				
Tetrahedral	Orth	.155	370	26.6	4444	22103	32660	15000
	Skew	.069	441	67.8				
Pyramid	Orth	.188	800	85.2	7444	35773	46330	18000
	Skew	.155	919	206.3				
Tet–pyr	Orth	.181	462	72.8	4444	22130	29660	12000
	Skew	.376	552	89.8				
Tri–prism	Orth	.212	339	20.4	4444	14893	16360	6000
	Skew	.101	362	35.5				

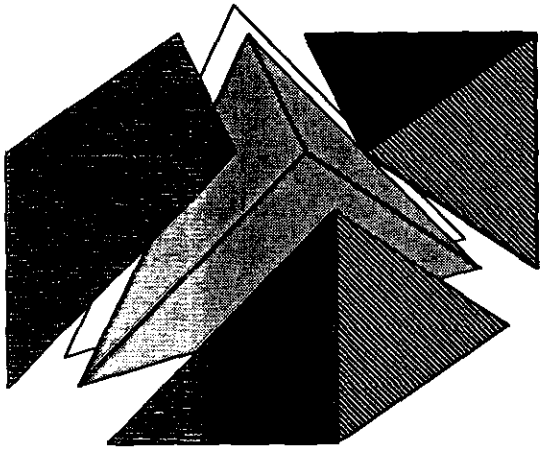

FIG. 10. *Hexahedral cell subdivided into five tetrahedrons.*

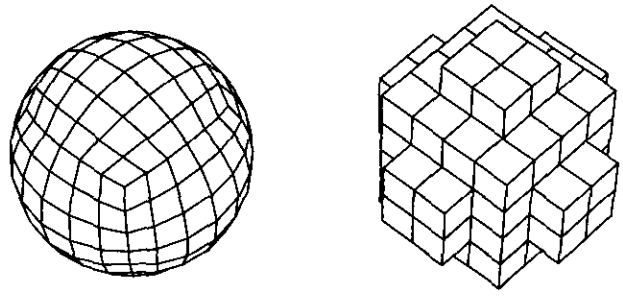

FIG. 12. Surface discretizations of a 0.1 m radius perfectly conducting sphere: (a) boundary conforming DSI surface grid (left); (b) stair-stepped orthogonal FDTD grid (right).

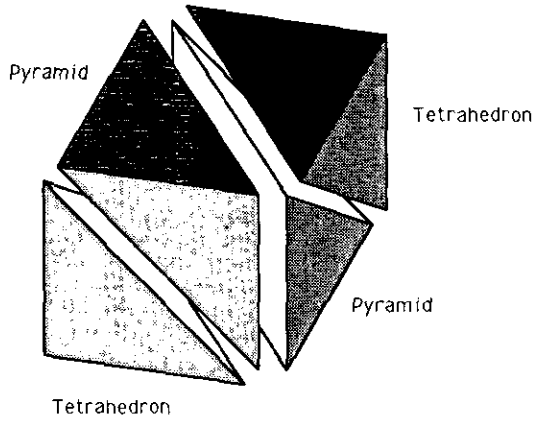

FIG. 11. Hexahedral cell subdivided into two tetrahedrons and two pyramids.

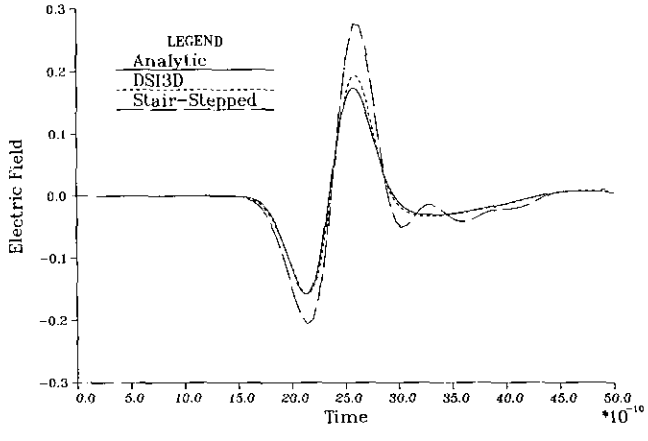

FIG. 13. Comparison of the DSI numerical solution and the stair-stepped orthogonal grid FDTD solution with the analytic solution for a point in the shadow region two sphere radii from the scatterer.

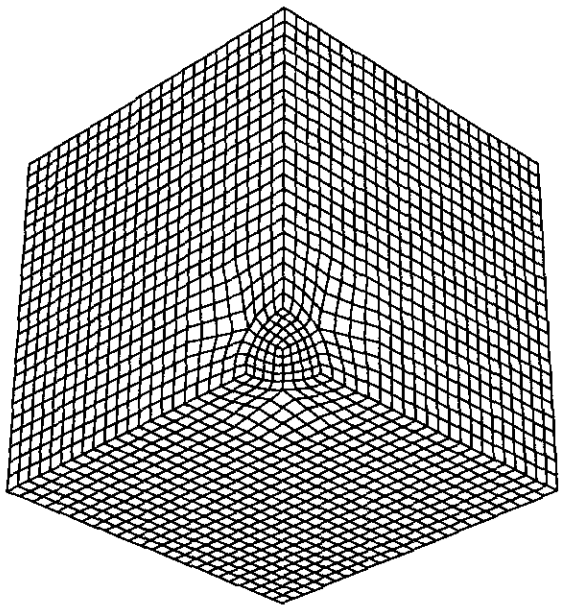

FIG. 14. Mostly orthogonal DSI grid for the dipole problem with a non-orthogonal region transitioning from a spherical surface.

and its first two derivatives, we have chosen the function to have smooth second derivatives. The analytic solution may be found in almost any standard text or in [15]. To solve this problem, we use a grid that is mostly orthogonal, but in the corner nearest the origin we use a small volume of non-orthogonal cells which transition from a spherical surface to the cubical grid. Figure 14 shows the grid used. We excite the problem by specifying the tangential components of the analytic solution on the spherical boundary surface and compare the numerical solution with the analytic solution at a point just outside of the non-orthogonal region. Figure 15 compares the E_z component of the DSI solution with the analytic solution for a point located

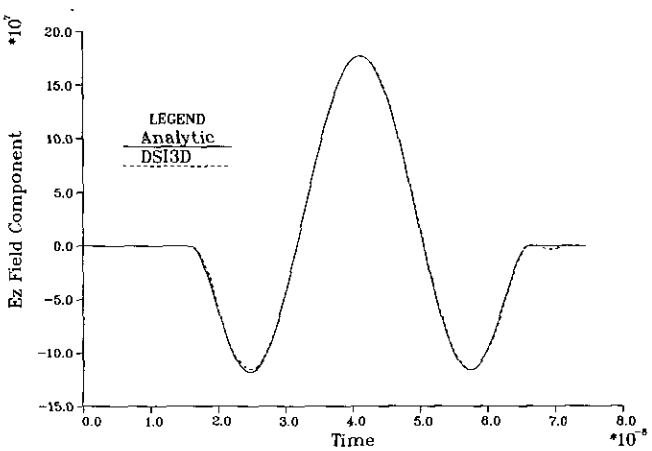

FIG. 15. Comparison of the E_z component of the DSI and analytic dipole solutions for a point just outside the non-orthogonal grid region.

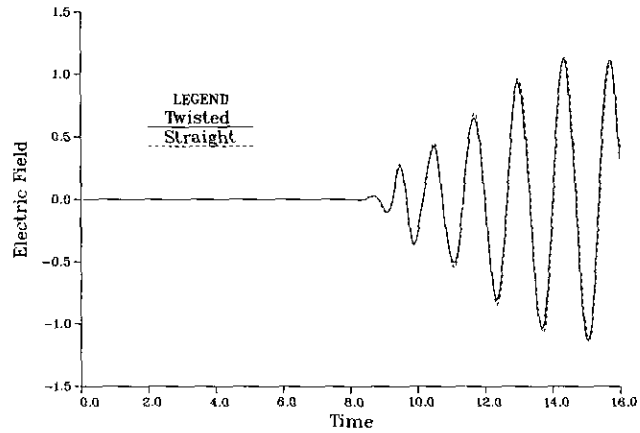

FIG. 16. Comparison of the electric field time histories for the twisted waveguide DSI numerical TE_{10} solution with a non-twisted waveguide DSI numerical solution at a point in the center of the guide immediately beyond the twisted portion.

slightly outside of the non-orthogonal cell region. We see that excellent results are obtained. The other solution components exhibit comparable accuracy.

As a final example we consider the problem of computing a TE_{10} waveguide solution for the rectangular waveguide (shown in Fig. 1) which goes through a 180° twist. This problem cannot be effectively solved using a stair-stepped orthogonal grid finite difference algorithm unless a tremendously large number of cells are used. The analytic solution for this problem is not known. However, from actual waveguide experiments, we know that a TE_{10} mode should propagate and be rotated 180° with little distortion by such a waveguide. Figure 1 shows the $10 \times 100 \times 3$ cell DSI grid used and Fig. 16 compares the DSI solution time history for a point in the center of the waveguide immediately after the twist with a TE_{10} solution for a similarly discretized waveguide with no twist. We note that the waves transition the twist with little distortion. Conversion of the TE_{10} mode to other modes does not occur because of the thinness of the waveguide. This problem was excited using the driving function (14).

CONCLUSIONS

The numerical results presented here lead us to believe that the DSI method presented in this paper is one with significant advantages. First, it is a direct generalization for unstructured non-orthogonal grids of the well-known and widely used orthogonal grid FDTD method for Maxwell's curl equations, so its approximation properties on regular orthogonal grids are quite well understood. Second, the DSI method is conditionally stable even for highly distorted grids. This is a distinct improvement when compared with our previous MFV algorithm. Third, the DSI method is conservative in that it conserves the divergence of the fields both locally and globally. Fourth, it is quite

accurate (comparing well with our previous MFV algorithm), even when used with irregularly structured grids. Fifth, it is very flexible and can be used with various combinations of different polyhedral discretizations.

The most significant disadvantage of the DSI method is the larger amount of information (primary grid structure plus dual grid structure) that is required. This disadvantage can largely be overcome by using discrete grids which are primarily composed of orthogonal hexahedral cells, together with a relatively few number of irregularly shaped non-orthogonal cells which are used to match boundaries more accurately. Implementing the algorithm in a two-phase way, where all of the geometry information is processed first and condensed into a dependency graph and related coefficients, allows one to take advantage of grid orthogonality when it occurs and also mitigates the extra non-orthogonal grid costs.

ACKNOWLEDGMENTS

The author would like to acknowledge many fruitful conversations concerning this work with Richard Ziolkowski, Scott Ray, Dale Nielsen, Jr., Richard Sincovec, and David Mackay. This work was performed under the auspices of the U.S. Department of Energy by the Lawrence Livermore National Laboratory under Contract W-7405-ENG-48, and also supported by RIACS/USRA and NASA via Cooperative Agreement NCC 2-387.

REFERENCES

1. K. S. Yee, *IEEE Trans. Antennas Propag.* **AP-14**(3), 302 (1966).
2. A. Taflove and M. E. Brodwin, *IEEE Trans. Microwave Theory Technol.* **MTT-23,** 623 (1975).
3. R. Holland, *IEEE Trans. Nucl. Sci.* **NS-24,** 2416 (1977).
4. K. S. Kunz and K. M. Lee, *IEEE Trans. Electromagn. Compat.* **EMC-20,** 328 (1978).
5. A. Taflove and K. R. Umashankar, *J. Elec. Waves Appl.* **1**(3), 243 (1987).
6. R. Holland, "The Case Against Staircasing," in *Proceedings, 6th Annual Review of Progress in Applied Computational Electromagnetics, March 1990,* p. 89 (unpublished).
7. R. Holland, *IEEE Trans. Nucl. Sci.* **NS-30,** 4589 (1983).
8. M. Fusco, *IEEE Trans. Antennas Propag.* **38**(1), (1990).
9. N. K. Madsen and R. W. Ziolkowski, *Wave Motion* **10,** 583 (1988).
10. J. Ambrosiano, S. Brandon, and R. Lohner, "Electromagnetic Propagation on an Unstructured Finite Element Grid," in *Proceedings, 6th Annual Review of Progress in Applied Computational Electromagnetics, March 1990,* p. 155 (unpublished).
11. A. Taflove and K. R. Umashankar, *Electromagnetics* **10**(1–2), 105 (1990).
12. V. Shankar, A. H. Mohammadian, and W. F. Hall, *Electromagnetics* **10**(1–2), 127 (1990).
13. N. K. Madsen and R. W. Ziolkowski, *Electromagnetics* **10**(1–2), 147 (1990).
14. G. Mur, *IEEE Trans. Electromagn. Compat.* **EMC-23,** 1073 (1981).
15. R. W. Ziolkowski and N. K. Madsen, *J. Comput. Phys.* **50**(3), 360 (1983).